Preparation and characterization of Ce-ZrO2/Al2O3 composites by DLP-based stereolithography

Original
Preparation and characterization of Ce-ZrO2/Al2O3 composites by DLP-based stereolithography / Inserra, B., Coppola, B., Montanaro, L., Tulliani, J.m., Palmero, P.. - In: JOURNAL OF THE EUROPEAN CERAMIC SOCIETY. - ISSN 0955-2219. - 43:7(2023), pp. 2907-2916. [10.1016/j.jeurceramsoc.2022.08.037]

Publisher:
Elsevier

Published
DOI:10.1016/j.jeurceramsoc.2022.08.037

Preparation and characterization of Ce-ZrO_2/Al_2O_3 composites by DLP-based stereolithography

Barbara Inserra, Bartolomeo Coppola, Jean-Marc Tulliani, Laura Montanaro and Paola Palmero

[1] Politecnico di Torino, Department of Applied Science and Technology, INSTM R.U. Lince Laboratory, Corso Duca degli Abruzzi, 24, Italy

* Corresponding author: paola.palmero@polito.it

Abstract

This work investigates the printability of Ce-ZrO_2/Al_2O_3 composites through a Digital Light Processing (DLP) technology. Commercially available 10 mol% CeO_2 and 12 mol% CeO_2-stabilized zirconia were mixed with alumina powders, to provide 11mol% CeO_2-stabilized ZrO_2/16 vol% Al_2O_3 (ZA_{16}) composite material. The powders were dispersed under wet conditions, and the homogeneous nanometric dispersion was maintained once added into the liquid monomer. Slurries at several solid loadings were explored, with and without dispersant addition. First, the key role of the dispersant to significantly enhance the solid loading and thus the sintered density was demonstrated. Second, among different dispersant-added slurries at various solid loadings, ranging from 65 to 80 wt%, the best compromise between rheological behaviour and curing depth was established. The best formulations, comprised between 70 and 80 wt%, successfully provided fully dense and completely homogeneous composites.

Keywords: Stereolithography, Digital Light Processing; 3D printing; zirconia-alumina composites; Microstructure; Mechanical properties

1. Introduction

Vat-photopolymerization methods, which include Stereolithography (SLA) and Digital Light Processing (DLP), are the most advanced additive manufacturing technologies for structural ceramics[1] ~~[rif~~], such as alumina and zirconia. While alumina is characterized by high hardness and wear resistance[2] ~~[rif]~~, yttria (meta)stabilized tetragonal zirconia (Y-ZrO_2) possesses outstanding bending strength and high fracture toughness[3] ~~[rif]~~, mainly due to the stress induced tetragonal-to-monoclinic (*t*-to-*m*) transformation[4,5] ~~[rif]~~. However, Y-ZrO_2 is affected by ageing (also known as low temperature degradation, LTD), meaning an uncontrolled *t*-to-*m* ZrO_2 phase transformation under moisture conditions, which compromises the use of pure Y-ZrO_2 ceramics into hydrothermal environment, including the biomedical applications[6] ~~[rif]~~. Composites in the alumina-zirconia system show a strategic combination of the above properties that - besides full biocompatibility towards human tissues - makes them an excellent choice for load-bearing biomedical applications, especially in the orthopaedics and dental fields, with a very limited sensitivity to LTD[7] ~~[rif]~~. Recently, ceria-stabilized zirconia (Ce-ZrO_2) and its composites are attracting increasing interest, due to the stability under moisture environment and to the pronounced stress-induced transformation toughening[8] ~~[rif]~~. To improve strength, fine second-phase particles such as alumina are typically added, providing ceramics characterized by a unique combination of high strength and fracture toughness[9–11] ~~[rif]~~.

For decades, alumina-zirconia ceramics have been manufactured using traditional ceramic shaping processes, such as dry pressing, isostatic pressing, slip-casting, gel-casting[12] ~~[rif]~~, tape-casting [13–16] and injection molding [17]. However, these traditional manufacturing processes cannot be used to fabricate components with complex geometries (internal holes, sharp corners, etc.) or parts that require high geometrical accuracy; in addition, post-production machining, such as cutting and surface polishing [18–20] are always necessary. Vat-photopolymerization techniques allow to overcome the above limits. In spite numerous studies focus on alumina [21–30] or zirconia [31–40], few studies have been dedicated to Al_2O_3 - ZrO_2 composites [41–45], and a single previous paper, to the best of the authors' knowledge, deals with Ce-ZrO_2-based composites fabricated by SLA or DLP[46] ~~[rif~~].

DLP has to face some main challenges, especially the preparation of a slurry with the required solid loading and rheological characteristics and the optimization of the printing process. The ceramic slurry needs to be homogeneous, stable and with a high solid loading: this reduces the shrinkage during sintering and improves the density of the final parts, providing them a high homogeneous microstructure, almost free of defects[47]. At the same time, the slurry has to be characterized by a low viscosity and a shear-thinning behaviour, to be easily spread on the tape during the progressive layer-by-layer building of the object. A further challenge for Ce-ZrO_2-based composites is related to the significant absorbance of ceria in the UV range[48,49] ~~[rif]~~, which reduces the light penetration within the slurry and thus the photo-polymerization effect.

In a previous work [41], alumina-zirconia slurries at different relative ratios were employed by mixing ready-to-use alumina and 3Y-ZrO_2 commercial slurries. Composite samples, at three compositions (15, 50 and 85 vol% ZrO_2), were optimized on the ground of fired density and microstructural development.

Compared to this previous work, aim of this research is to develop Ce-ZrO_2/16 vol% Al_2O_3 dense and homogeneous composites, through a careful preparation of printable slurries. Commercial Al_2O_3 and Ce-ZrO_2 powders were mixed and dispersed, and the homogeneous nanometric dispersion was maintained in the polymer slurry. Slurries at several solid loadings were explored, with and without dispersant addition. First, the key role of dispersant in significantly enhancing the solid loading and thus the sintered density was demonstrated. Second, among different dispersant-added slurries at various solid loadings, ranging from 65 to 80 wt%, the best compromise between rheological behaviour and curing depth was established. The best formulations, comprised between 70 and 80 wt%, successfully provided fully dense and completely homogeneous composites.

2. Material and methods

2.1 Materials

Ceria-stabilized zirconia (Ce-ZrO_2) and α-Al_2O_3 commercial powders were used to prepare the slurries. In particular, two grades of Ce-ZrO_2 powders (Daiichi Kigenso Kagaku Kogio Co. LTD, Japan) were used, containing 10 mol% (10Ce-ZrO_2) and 12 mol% (12Ce-ZrO_2) of ceria in the zirconia lattice. The powders were characterized by an average grain size of 0.8-1.1 µm, as declared by the producer, and a specific surface area of 14.3 m^2/g.

α-Al_2O_3 powder (TM-DAR TAIMICRON, Taimei Chemicals Co., Japan) was characterized by primary particle size of about 150 nm, a specific surface area of 14.5 m^2/g and particle density of 3.96 g/cm^3.

The photocurable commercial resin (Admatec Europe BV, The Netherlands) consists of a monomer resin system with a photoinitiator, diphenyl(2,4,6,-trimethylbenzoyl)phosphine oxide, and acrylates. A commercial dispersant (Disperbyk-103, BYK Chemie, Germany) was used to improve stability and enhance slurries solid loading.

2.2 Slurry preparation

A mixture of 10Ce-ZrO_2, 12Ce-ZrO_2 and α-Al_2O_3 powders was prepared, in order to develop a composite having the following composition: 11Ce-ZrO_2/16vol% Al_2O_3 (labelled as Ce-ZA_{16}). 10Ce-ZrO_2 and 12Ce-ZrO_2 powders were mixed at 50 wt%, in order to provide 11 mol% CeO_2 stabilizer in the zirconia lattice, according to previous results[10,11] ~~[rif]~~. A zirconia ethanol suspension, prepared at a solid loading of 33 wt%, was dispersed by ball milling for 18 h. Zirconia spheres (Tosoh Corporation, 2.0 mm in diameter, weight ratio of 1:5 with respect to the powder) were selected as milling media since they exhibit high crushing strength and wear resistance. The particle size distribution of the as-received powders and the dispersed mixture was checked by laser granulometry

(Mastersizer 3000, Malvern Panalytical, Worcestershire, UK). The suspension was then oven dried at 60° C for 12 h.

For the elaboration of the polymer slurries, the dried Ce-ZA$_{16}$ composite powders were added to the acrylic photoreactive resin ranging from 50 to 80 wt% (corresponding to about 16– 42.5 vol%) ceramic powder loading. Two sets of slurries were prepared: the former, at solid loadings ranging from 50 to 62.5 wt% were dispersant-free; the latter, in the range 65-80 wt% were prepared with the addition of 1.0 – 4.0 wt% dispersant (as respect to the dry powder). The dispersant was added to the liquid monomer under mechanical stirring, for 15 minutes. Then, Ce-ZA$_{16}$ powder was added to this mixture, little by little to avoid the formation of agglomerates, always under stirring, for other 30 minutes. In the end, the obtained slurry was milled in agate jars with agate spheres (d = 10 mm) for 3 h at 350 rpm in a planetary miller (Fritsch Pulverisette, Fritsch GmbH, Germany). The slurry was then de-aired for 1 hour under vacuum. The rheology of the slurries was studied using a rotational rheometer (Kinexus Pro+, Netzsch Geraetebau GmbH, Selb, Germany) equipped with stainless steel parallel plates (20 mm diameter) with a 1 mm gap between plates by applying shear rates of 0.1–1000 s^{-1} at 25 °C.

2.3 Digital Light Processing (DLP)

Bar-shaped specimens were designed using the AutoCAD software with dimensions of 15×5×5 mm^3 for dilatometric analysis and 32×3×4 mm^3 which are appropriate for three-point bending tests. Samples were printed using a DLP-based stereolithographic printer (ADMAFLEX 130, ADMATEC Europe BV, TheNetherlands), which operates with a 405 nm wavelength UV light. It is essential to investigate the curing properties, such as the curing depths and curing degrees of the UV-curable suspensions. The main printing parameters were optimized with several tests with the goal to find the best compromise between high resolution, adhesion on the substrate, and uniformity of each layer. These are crucial specifications that, if not appropriately selected, lead to severe delamination and compromise the integrity of the entire sample, most of all the mechanical properties. The most reliable parameters were found in a layer thickness, exposure time, and LED power fixed at 20 µm, 12 s and 31.96 mW/cm^3 respectively. A delay of 50 s before exposure is needed to let air bubbles be removed from the slurry. A 125 µm doctor blade was used. In order to determine the curing depth, slurries were submitted to the UV light for different exposure times. The cured layers in a chessboard configuration were cleaned with paper to remove the uncured slurry and the thickness of the single-layer was measured with a digital micrometer.

After printing, the green bodies were submitted to a water debinding process for 24 h, to remove extra slurry, and left overnight at room temperature. Then, the samples were oven-dried at 70 °C for 6 h before being submitted to thermal debinding and sintering processes.

2.4 Post-processing and sintering

The debinding and sintering processes were performed according to the thermal cycle displayed in **Figure 1**, using an electric furnace (Carbolite 1800, Carbolite Gero GmbH) under air atmosphere.. The slow heat treatment avoids cracking during resin decomposition. The sintering behaviour of the printed bars was investigated by dilatometry analysis, according to the thermal cycle in Figure 1. The sintered density was calculated according to the theoretical density (TD) of Ce-ZA$_{16}$ (5.87 g/cm^3).

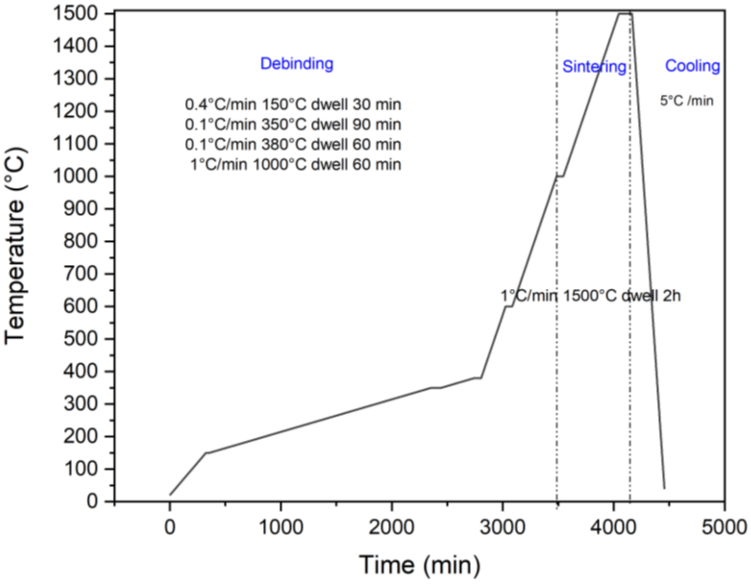

Figure 1. Schematic diagram of thermal debinding and sintering cycles

2.5 Characterizations

The density of the ceramic parts, ρ (g/cm^3), was determined by buoyancy method, following Archimedes' principle (Density Determination Kit, Sartorius YDK01, Göttingen, Germany). The microstructures of the green and sintered bodies were characterized by means of a FE-SEM (Hitachi, Tokyo, Japan). The surfaces of the sintered samples were polished down to 1 µm with diamond paste and thermal etched at a temperature 100 °C below sintering temperature (heating rate of 10 °C/min, with 10 min dwell). Then, the samples were platinum sputtered before FE-SEM observations. The grain size of both Al_2O_3 and Ce-ZrO_2 phases were determined by means of image analysis software (Scandium by Soft Image System) on about 300 grains. for composite material and sintering temperature.

Crystalline phases identification was carried out by XRD analysis performed on the sintered samples using a Pan'Analytical X'Pert Pro instrument (Pan'Analytical, The Netherlands) with CuKα radiation (0.154056 nm) in the 2 θ range 5-70°. Phases were identified by JCPD file n 82-1398 for the tetragonal zirconia phase stabilized with ceria, and 74-0815 to identify the monoclinic zirconia phase. The intensities of the monoclinic (-111) and (111) peaks and the (101) tetragonal peak were integrated to calculate the volume of monoclinic zirconia in the composites, according to the Garvie Nicholson method.

3. Results & discussion

3.1 Powders characterization

The particle size distributions of as-received α-Al_2O_3, 10Ce-ZrO_2 and 12Ce-ZrO_2 powders are depicted in **Figure 2(a)**. While 10Ce-ZrO_2 and 12Ce-ZrO_2 powders are characterized by similar bimodal distributions, α-Al_2O_3 powder shows an almost monomodal distribution, but displayed at significantly larger values. The D_{10}, D_{50} and D_{90} values, which correspond to 10, 50 and 90% of the cumulative volume distribution, are collected in **Table 1**, and underline the remarkable difference in the particles' starting agglomeration. In spite of this, after ball-milling, the mixture achieved a monomodal and fine distribution, as depicted in **Figure 2(b)** (black lines), with D_{50} and D_{90} values of about 0.3 and 0.5 µm, respectively (Table 1). Once dried, the composite powder was dispersed again into ethanol for few minutes, and its agglomeration degree checked a second time by laser granulometry. As depicted in **Figure 2(b)** (red lines), the particles size distribution as well the D_{10}, D_{50} and D_{90} (**Table 1**) are close to the that of the dispersed alcoholic suspension, showing that only a soft agglomeration occurred during drying.

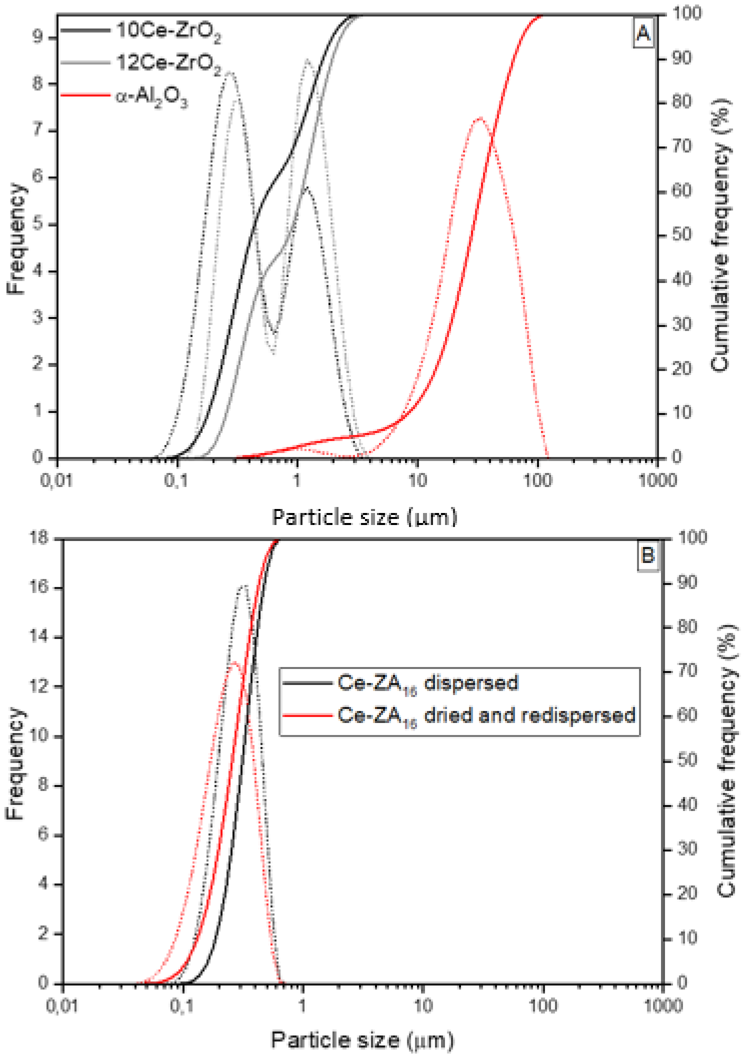

Figure 2: Particle size distribution of: **(a)** as-received 10Ce-ZrO$_2$ (dark lines), 12Ce-ZrO$_2$ (grey lines) and α-Al$_2$O$_3$ (red lines); **(b)**: Particle size distribution of Ce-ZA$_{16}$ mixed powders after 18 h of dispersion (black curve) and of the same powder after drying and re-dispersion (red curve). Frequency (solid lines) and cumulative frequency (dotted lines) are depicted in both figures.

Table 1: Particle size (µm) corresponding to 10% (D$_{10}$), 50% (D$_{50}$) and 90% (D$_{90}$) of the cumulative distribution of as-received 10Ce-ZrO$_2$, 12Ce-ZrO$_2$, α-Al$_2$O$_3$ powders, as well as of the dispersed Ce-ZA$_{16}$ composite powder.

	D_{10} (µm)	D_{50} (µm)	D_{90} (µm)
As-received $10Ce-ZrO_2$	0.18	0.41	1.62
As-received $12Ce-ZrO_2$	0.26	0.84	1.94
As-received α-Al_2O_3	8.22	28.30	62.10
Dispersed Ce-ZA_{16} mixture	0.19	0.31	0.47
Dried and re-dispersed Ce-ZA_{16} mixture	0.13	0.26	0.43

3.2 Preliminary set-up of the slurries

As preliminary attempts, dispersant-free slurries were prepared at 55.0-62.5 wt% solid loadings. The evolution of the shear viscosity as a function of the shear rate is depicted in **Figure 3**. All the tested slurries showed a shear-thinning behaviour, with a marked viscosity decrease as the shear rate increases. In fact, as the level of shearing stress is gradually increased, the structural units respond to the applied stress by aligning themselves in the direction of flow which facilitates bulk flow in the system[50] ~~[rif]~~. Such behaviour is the one required in the stereolithography process, as it assures the slurry being spread on the tape evenly[51] ~~[rif]~~. In addition, as the solid loading increased moving from 55.0 wt% to 62.5 wt%, an expected displacement of the shear viscosity curves at higher values was observed, due to an increased inner friction of the ceramic particles.

Besides the necessary shear-thinning behaviour, it is important to check the shear viscosity at the operative shear rate, which corresponds to the shear rate applied by the blade on the slurry during its spreading, that was identified at 160 s^{-1} in our process, providing shear viscosity of 0.6, 0.7, 1.3 and 2.2Pa·s, respectively, for the slurries at 50, 55, 60 and 62.5 wt% solid loadings. To make a comparison, Zheng et al.[42] ~~[rif]~~ successfully printed alumina-zirconia composites at the shear viscosity of 0.4 Pa.s at the shear rate of 18.6 s^{-1}. Previous literature provides appropriate values of the shear viscosity, at the operative working rate, to achieve good printability. For alumina-zirconia composites, it was reported that the viscosity of the ceramic suspension for SLA should be less than 3 Pa.s (at the working shear rate) to ensure its flowability[52] ~~[rif]~~. However, it seems that the viscosity of 5 Pa·s at the working shear rate can be properly considered as the upper limit [53] ~~[rif]~~, i.e. the ultimate acceptable viscosity for printing ceramics by vat-photopolymerization technologies. In our case, although all the slurries showed viscosity lower than the limit value, that of the most charged formulation was close to the value of 3 Pa.s, indicating that the maximum solid loading was already achieved.

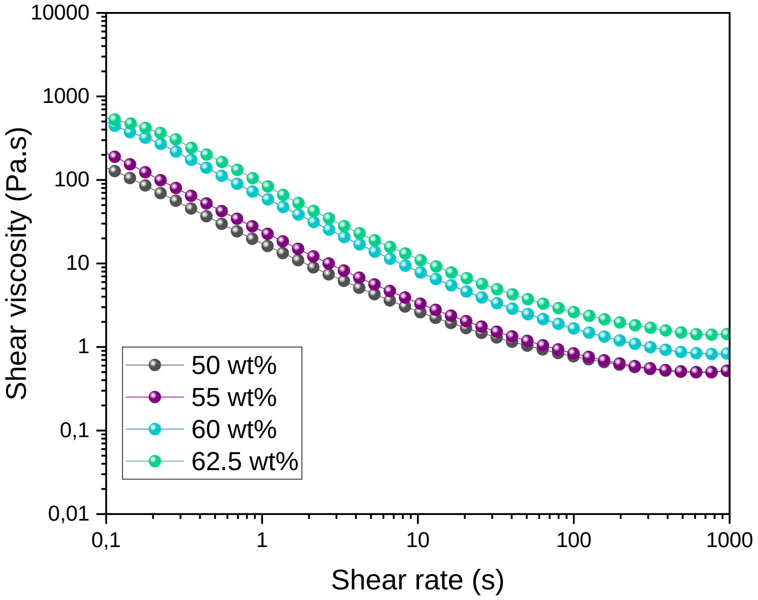

Figure 3: Rheological curves of Ce-ZA$_{16}$ slurries, prepared at 55-62.5 wt% solid loadings.

In **Figure 4**, the evolution of the curing depth as a function of the exposure time to UV irradiation is depicted, as a key parameter to assess the printability of a photocurable slurry. For all the slurries, a reasonable increase of the curing depth with an increased exposure time can be observed. However, this happens at progressively lower rate with the increase of solid loading. At a given exposure time, the UV penetration in slurries at increasing solid loadings is significantly reduced.

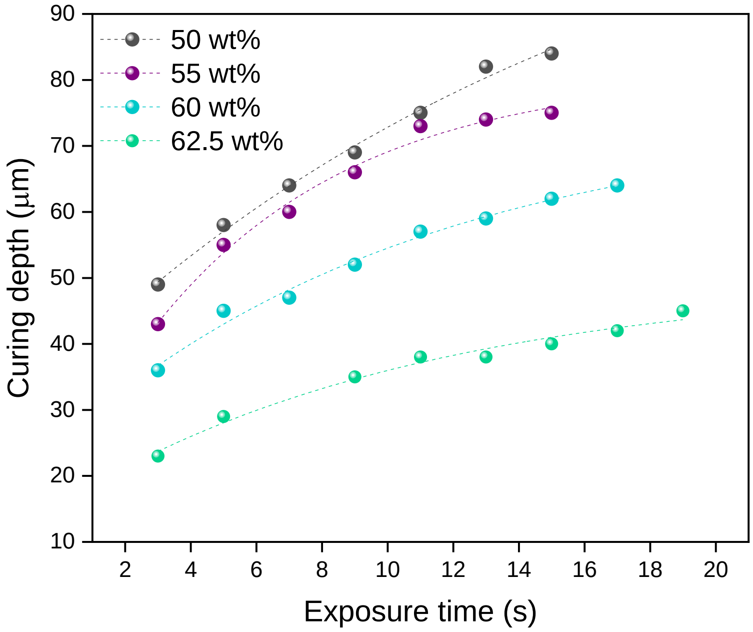

Figure 4: Curing depths (at 31.96 mW/cm^2) as a function of exposure time for slurries at 55.0-62.5 wt% solid loadings

The decreased UV penetration at increased solid loading can be imputed to two different factors. On one side, the increased amounts of ceramic particles induce a higher light scattering, due to refractive index mistmach between the resin and the ceramic particles[46] ~~[rif]~~. On the other side, the presence of 11 mol% ceria in the mixture and its significant UV-absorbance has to be considered. Ceria is a well-known ultraviolet blocking material, that strongly absorbs in UV-C (100–280 nm), UV-B (280–315 nm) and UV-A (315–400 nm) light regions[46,54] ~~[rif]~~.

While a low solid loading is beneficial in terms of viscosity and curing depth, which assure the formulation to be printable, a high solid loading is required to reach high green density in the printed parts, to reduce the shrinkage during drying and sintering, and to achieve high fired density in the sintered pieces. In **Figure 5**, the fired density (at both 1500 °C/1h and 1550 °C/1h) of sintered parts fabricated with the slurries at 55.0-62.5wt% solid loadings is displayed. The increase of the sintering temperature from 1500 °C to 1550 °C allows a 2-3% increase of the fired density. At both sintering temperatures, the same trend can be observed, with a progressive increase of the density up to 60 wt%, followed by a decreased density at 62.5 wt%. Maximum density values for the 60wt% slurry were 95.1 ± 1.1% and 97.6 ± 0.9% at 1500 °C/1h and 1550 °C/1h, respectively. In **Figure 6**, some FESEM micrographs of the 60 wt% solid loading material, sintered at 1500 °C/1h, are depicted. The lower-magnification image (a) shows the presence of several flaws, probably imputed to the printing process (i.e., not optimal slurry viscosity) as well as to binder burn-out. When the sintering temperature was increased to 1550 °C/1h (images not shown), the same flaws were present, even if in a reduced amount. However, the higher magnification micrograph (b) shows a very homogeneous microstructure, with an even distribution of alumina and zirconia grains into the composite material.

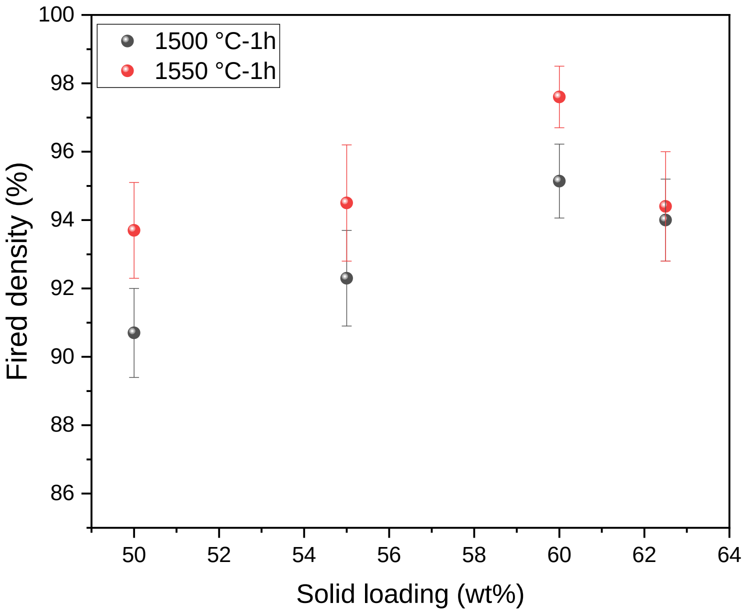

Figure 5: Fired density (calculated by the buoyancy method, and related to materials theoretical density) as a function of the slurries solid loadings

Due to the relatively low fired density of the samples and the microstructural flaws, the formulations were further optimized through the addition of a dispersant (Disperbyk 103), which allowed a significant increase of the solid loading, as descrived in the following paragraph.

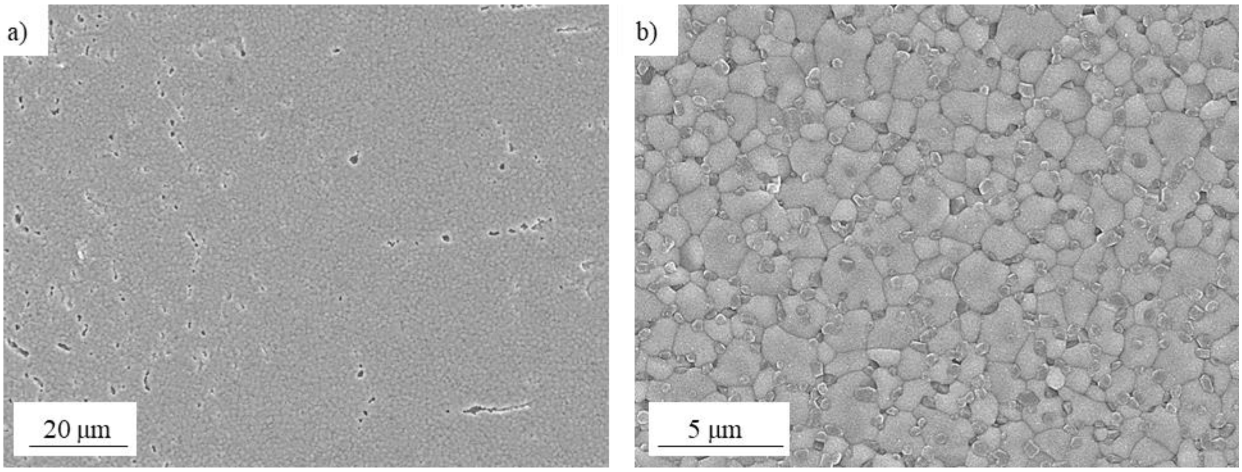

Figure 6: FESEM micrographs of the sample at 60 wt% solid loading and sintered at 1500 °C/1h

3.3 Optimization of the slurries: effect of dispersant amount and solid loading

Addition of 1.0-4.0 wt% dispersant to the slurries allowed to achieve solid loadings in the range 65-80 wt%. Precisely, slurries at 65, 68, 70, 73, 78 and 80 wt% were prepared, while the dispersant amount was optimized for each slurry through rheological tests, as shown in **Figure 7** for the highest solid loading slurries (70-78 wt%).

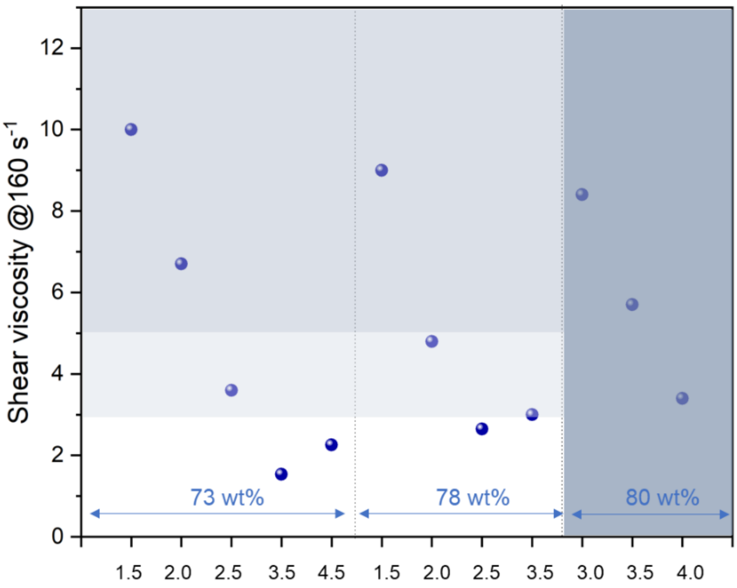

Figure 7: Shear viscosity at the operative shear rate (160 s^{-1}) as a function of the dispersant amount for the 70, 73 and 78 wt% slurries. Light and medium grey areas denote the printability limits due to a not proper viscosity, while the dark grey area denotes the not the printability limit due to too low curing depth.

While for the 80 wt% slurry, the viscosity progressively decreased by increasing the dispersant amount, for the 73 and 78 wt% formulations a minimum shear viscosity was reached at a specific dispersant amount, after which the viscosity increased again. This behaviour has been already reported in literature, and is associated to the fact that a dispersant excess may introduce unwanted polymer tangles between ceramic particles, thus leading to agglomeration and viscosity increase[55,56] ~~[rif]~~. Starting from the above graphic, for each formulation, the optimal dispersant amount – corresponding to the lowest shear viscosity – was determined, as reported in **Table 2**. Further, we can observe that some of the dispersant additions did not allow to decrease the viscosity below the previously reported limits, which range between 3 and 5 Pa.s according to literature[52,53] [rif]. In our case, a viscosity higher than 5 Pa.s did not allow the slurry to be easily spread and thus printed, a homogeneous bubble-free layer is mandatory for successful printings.

~~Furthermore, the ceriated zirconia, which is a well-known UV-absorber, prevents to set of thick single layers of the printed sample. As the solid load increase, the light scattering increase, and more difficult is to go in deep for the UV light to polymerize the layer To obtain an equilibrium between high resolution and optimized polymerization the optimum thickness of each layer, according to our tests, was found to be 20 µm. For this reason viscosity values higher than 3 Pa.s allow the slurry to be spread, but with a not optimal viscosity, because is not easy to remove air bubbles from such a thin layer.~~

In addition, the ceriated zirconia, which is a well-known UV-absorber, prevents the polymerization of thick single layers during the printing process. As the solid load increases, the light scattering increases, and it is more difficult for the UV light to go in depth and polymerize thick layers. To reach a compromise between high resolution and optimized polymerization, the optimum thickness of each layer, according to our tests, was found to be 20 µm. For this reason, viscosity values higher than 3 Pa.s allowed the slurry to be spread, but not with an optimal viscosity, because some air bubbles remained entrapped in such a thin layer, as observed later during FE-SEM observations.

~~Further, we can observe that some of the dispersant additions did not allow to decrease the viscosity below the previously reported limits, which range between 3 and 5 Pa.s according to literature [52,53] [rif]. In our case, viscosity higher than 5 Pa.s did not allowed the slurry to be easily spread and thus printed, while values higher than 3 Pa.s allowed the slurry to be spread, but a not optimal viscosity could produce issues such as a not proper air removal during printing~~. This allows to determine a certain printability range for each formulation which corresponds to the white area in Figure 7. Under these conditions, homogeneous and stable slurries were obtained, which could be easily spread on the tape by the blade.

As previously mentioned, besides the viscosity, the curing depth plays a key role to assess the printability of the slurries. Taking as a reference the exposure time of 15 seconds, slurries at 70 and 73 wt% were characterized by curing depths higher than 35 μm, while the 80 wt% showed a value lower than 30 μm, which does not respect the minimum curing depth (equal to 1.5×layer thickness) necessary to avoid delamination. On the other side, a prolonged exposure time did not allow to increase the curing depth to acceptable values. Therefore, 80 wt% formulation was thus not printed, and was regarded as the upper limit in slurry solid loading.

Table 2: Compositional features of the slurries: solid loading (expressed as both weight% and volume%) and optimal dispersant amount

Solid loading (wt%)	Solid loading (vol%)	Dispersant (wt%)
65%	28.5	1.0

68%	28.9	1.0
70%	30.1	1.0
73%	33.4	3.5
78%	39.6	2.5
80%	42.5	4.0

Figure 8 (a) shows the evolution of green (a) and sintered (b) density at 1500 °C/1h and 1550 °C/1h (b) as a function of the solid loading. While the green density continuously increases with solid loading, the fired density increases up to achieve a plateau at 70 wt%. In addition, while the slurries at 65wt% and 70wt% significantly increased their sintered density moving from 1500 °C/1h to 1550 °C/1h, the higher solid loadings slurries just increased the density of 1-2%. The maximum density is achieved at 70 wt%, providing values of 97.3% and 99.4% at 1500 °C/1h and 1550 °C/1h, respectively.

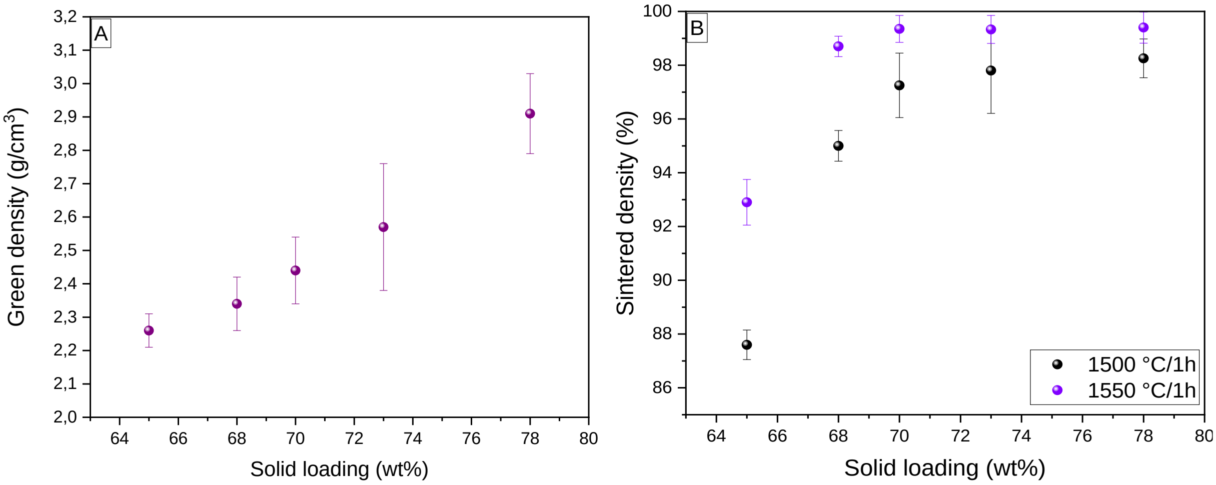

Figure 8: Green and sintered density as a function of the slurries solid loading. Printed samples sintered at 1500 °C/1h (black symbols) and 1550 °C/1h (violet symbols).

In order to investigate the microstructural evolution during sintering, a bar produced by the formulation at 73wt% solid loading and already submitted to thermal debinding, was characterized by dilatometric analysis (**Figure 9**). The sample was characterized by a green density of 2.49 g/cm^3. The onset sintering temperature occurred at about 1050 °C, while the inflection point at 1245 °C identified by the derivative curves shows the temperature of maximum shrinkage rate. At the end of the sintering cycle, a total shrinkage of 26% was recorded, providing a final density of 97.8%.

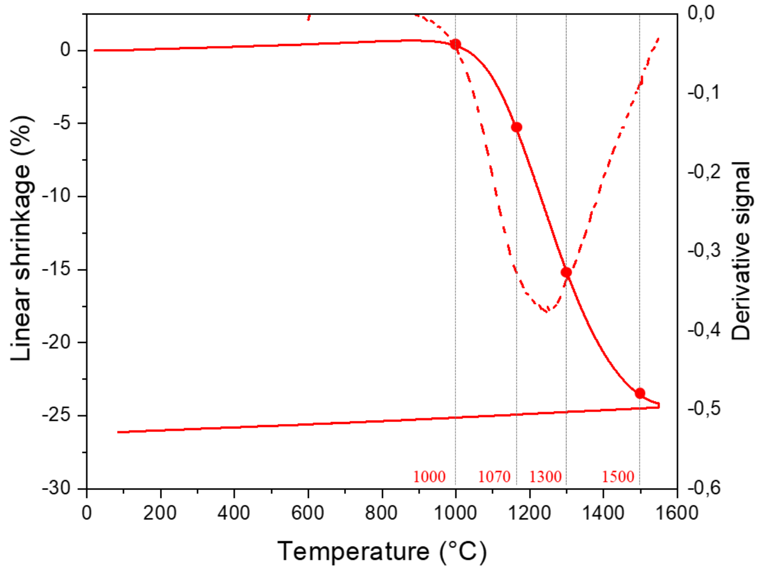

Figure 9: Linear shrinkage (solid line) and derivative (dotted line) curves of a printed bar from a 73 wt% solid loading slurry.

On the ground of the dilatometric curve and its derivative, the microstructural evolution of the printed samples at selected temperatures was investigated. Therefore, further printed samples were sintered at: *i*) 1000 °C, just before the sintering onset temperature; *ii*) 1170 °C, which corresponds to ~5% less shrinkage as respect to the value determined at the maximum shrinkage rate; *iii*) 1300 °C, which corresponds to ~5% more shrinkage as respect to the value determined at the maximum shrinkage rate; *iv*) 1500 °C, which corresponds to ~ 98% of the total linear shrinkage during the heating cycle. The fracture surfaces of the samples thermally treated at the above temperatures are provided in **Figure 10**, at lower (left) and higher (right) magnification. At 1000 °C, we can observe a homogeneous and compact microstructure, free from large defects. From 1170 °C to 1500 °C it is possible to observe the printed layers, showing defect-free interfaces (i.e., no cracks, no air bubbles, no delamination). The density progressively increased, reaching 51.0% TD at 1170 °C, 69.6%TD at 1300 °C and 95.5%TD at 1500 °C. At this last temperature, an average printed layer thickness of about 11 µm was determined~~, in agreement with the shrinkage occurring during the polymerising, debinding and sintering stages~~. Even if a high solid loading (higher than 45 vol%) is typically suggested for the stereolithography of ceramic slurries[46] ~~[rif]~~, the high fired density achieved and the whole microstructural evolution here depicted indicate that lower solid loadings – as those used in this work – are however appropriate.

The higher magnification images show the microstructural evolution of the fired samples: at 1000 °C, nanometric particles of about 100-200 nm in size can be observed, in good agreement with the starting particle size distribution. No particle agglomerates can be observed, suggesting that the homogenous and fine dispersion of the three starting powders was kept once added to the polymer fraction. Limited grain growth was observed at 1170 °C, with particles of 150 – 300 nm in size. In the samples calcined at 1300 °C and 1500 °C, alumina and Ce-ZrO_2 particles could be distinguished on the ground of their different size, with finer alumina grains and larger zirconia particles. At 1300 °C, a still limited grain growth occurred, giving rise to ultra-fine particles (average size of ~ 250 nm for alumina and ~ 450 nm for zirconia). On the opposite, an important grain growth occurred from 1300 °C to 1500 °C, providing micronic zirconia grains (~ 1 µm) and sub-micronic alumina particles (0.5 µm).

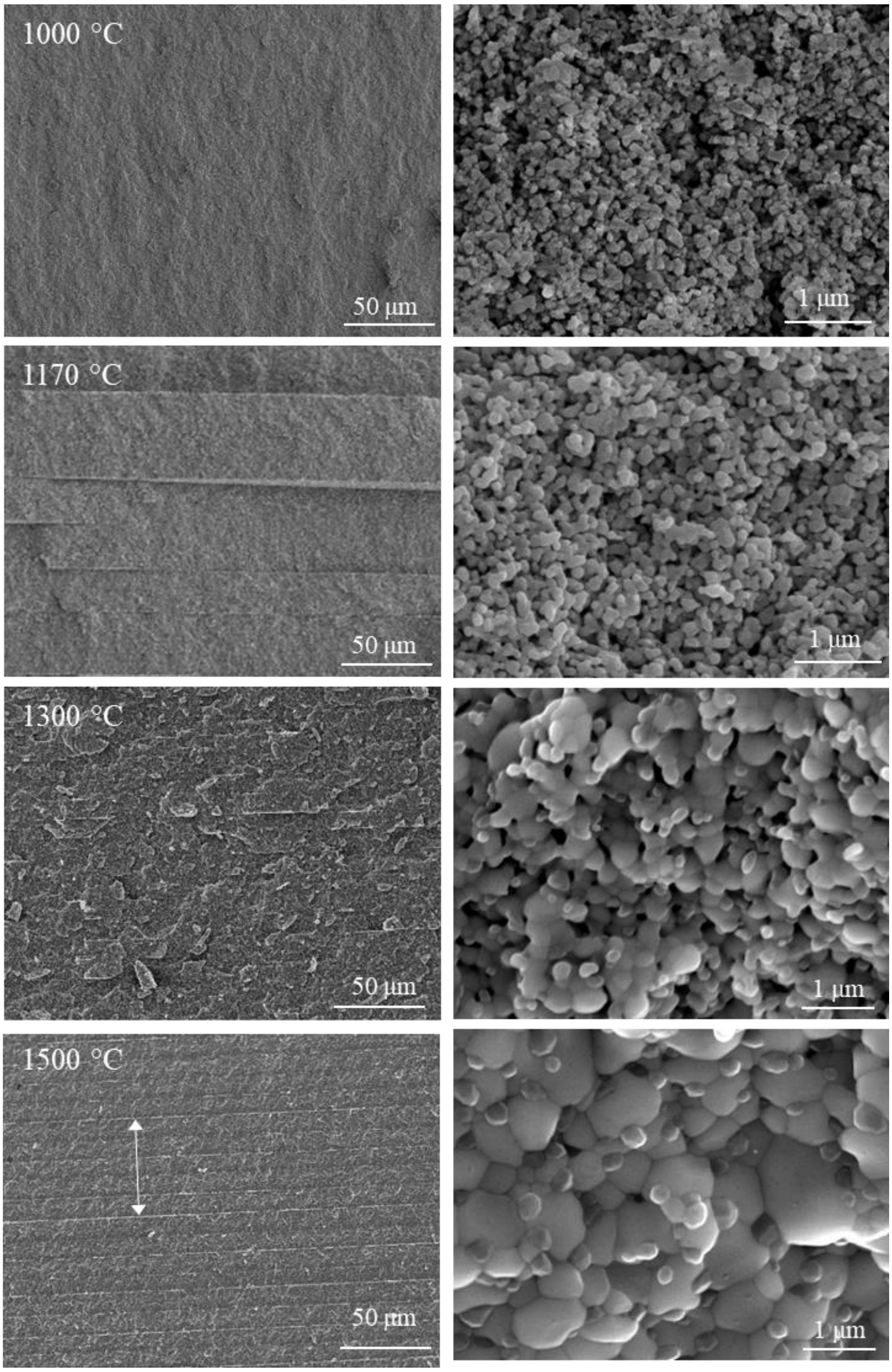

Figure 10: Microstructural evolution of printed samples (slurry at 73wt %) fired at different temperatures. Lower (left) and higher (right) magnifications images are depicted for each sample.

In **Figure 11**, some FESEM micrographs of the samples printed by slurries at 70, 73 and 78wt% (i.e., those reaching the higher final densities) sintered at 1500 °C/1h are shown. The lower magnification images (a, d, g) show a very compact and homogeneous microstructure, completely free from the flaws observed in the samples printed by the dispersant-free slurries (see Figure 6), clearly indicating that the addition of the dispersant and the consequent optimization of the rheological behaviour and reduced amount of the organic fraction were mandatory to eliminate the previous flaws. The higher magnification images (b-c, e-f, h-i) show homogeneous microstructures, with an even distribution of fine alumina grains into the zirconia matrix. ~~Also, a similar particle size for these three samples was observed. For instance, image analysis performed on the 73 wt% sample sintered at 1500 °C/1h provided an average grain size of …and of …for the zirconia and alumina phases, respectively, and of ….. for the same material sintered at 1550 °C/1h.~~ Also, a similar particle size for these three samples was observed. For instance, image analysis performed on the 73 wt% sample sintered at 1500 °C/1h provided an average grain size of 1.1 µm±0.3 µm and of 0.5 µm±0.1 µm for the zirconia and alumina phases, respectively. The same material sintered at 1550 °C/1h shows an average size of 1.2 µm±0.5 µm for the zirconia grains and 0.5 µm±0.1 µm for alumina grains.

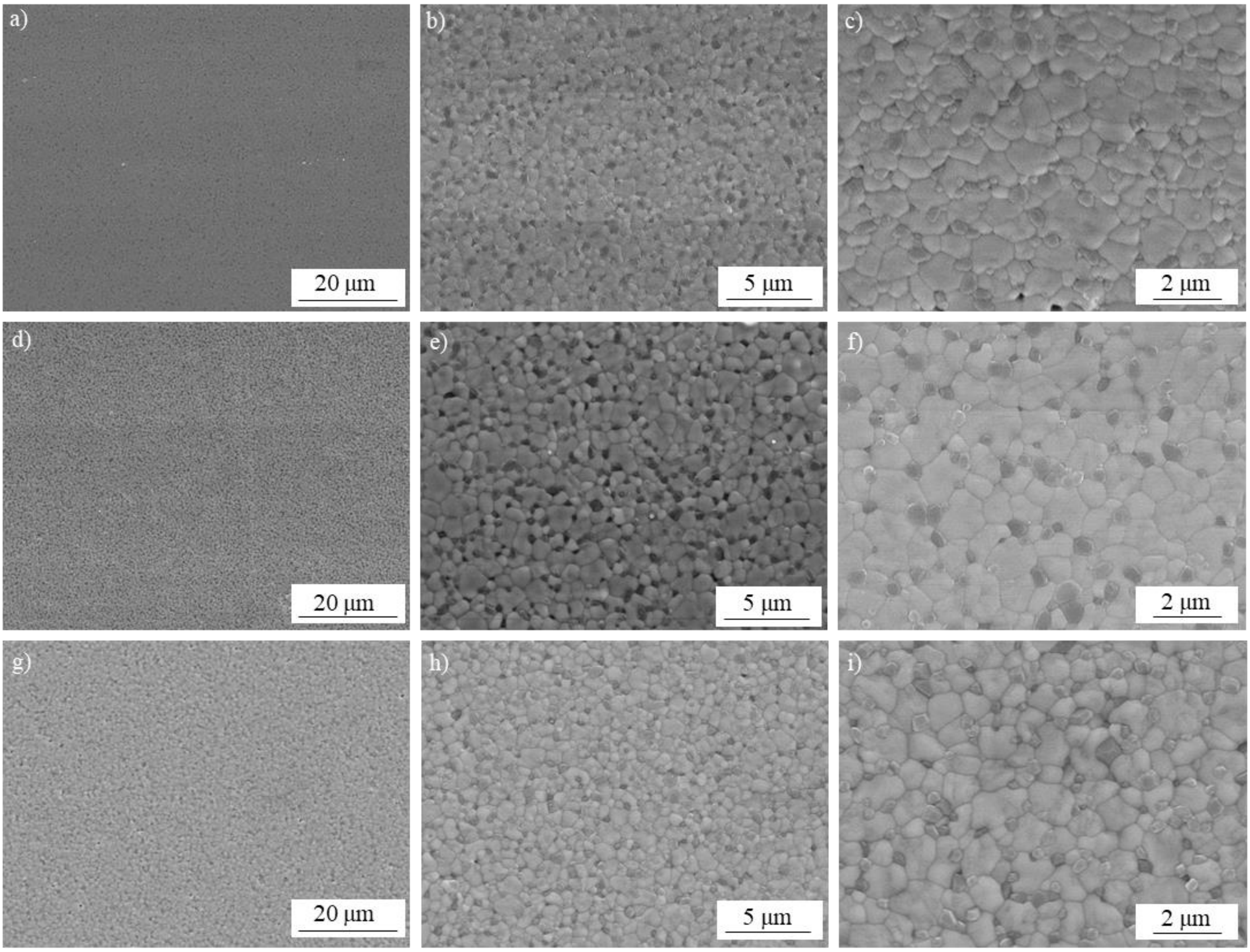

Figure 11: FESEM micrographs of sample printed from slurries at 70 (a-c), 73 (d-e) and 78 wt% (g-h) and sintered at 1500 °C/1h.

Finally, even if the small samples, as those fabricated for dilatometry, showed a compact and almost defect-free structures, the fabrication of longer bars for flexural tests showed some delamination between layers besides edge cracks (**Figure 12**). In fact, at higher aspect ratios, during drying and curing samples underwent a slight bending, which induced such flaws.

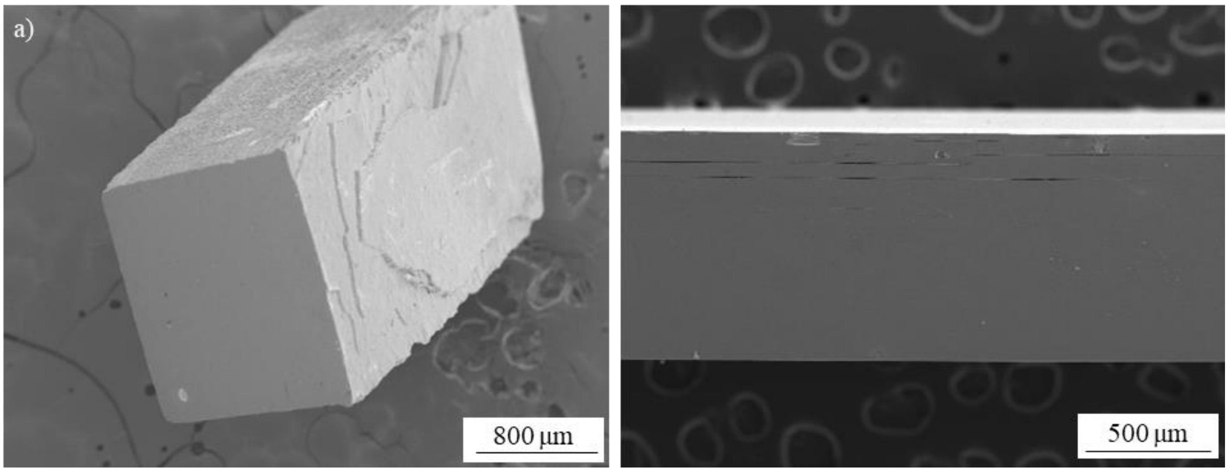

Figure 12: Cross-section (a) and lateral view (b) of samples printed at 73 wt% in different dimensions

In Figure 13 a comparison of the XRD patterns of the raw 10Ce-ZrO_2, 12Ce-ZrO_2, Al_2O_3 powders (light blue, blue, and green line respectively) with the Ce-ZA_{16} printed and sintered sample at 1500 °C/1h (red line) is depicted. For raw materials, tetragonal phase and monoclinic phase are observed in raw 10Ce-ZrO_2, 12Ce-ZrO_2 powder. A monoclinic volume fraction, Vm, of about 75% and 38% was determined in these two materials, respectively, by applying the Toraya equation. ~~The Toraya equation provided values of ….in these two materials, respectively~~. On the opposite, the printed and sintered composite showed almost pure tetragonal phase, indicating that the 11mol% ceria in the zirconia lattice was properly stabilize the tetragonal phase at room temperature. XRD performed on a fractured sample (tensile side) showed 78% monoclinic phase, suggesting that the stabilizer amount was proper to induce the correct stress-induced phase transformation.

On the ground of these succesful results, and namely: 1) a high fired density; 2) a fully homogenous microstrcture; 3) a correct zirconia transformability, next efforts will be dedicated to fabricate long bars suitable for mechancial properties measurements. As mentioned, preliminary results showed some delamination. Thus, an even more careful tailoring of the printing parameters (curing depth and exposure time will be performed) as well as post-processing will be the key to overcome such issue.

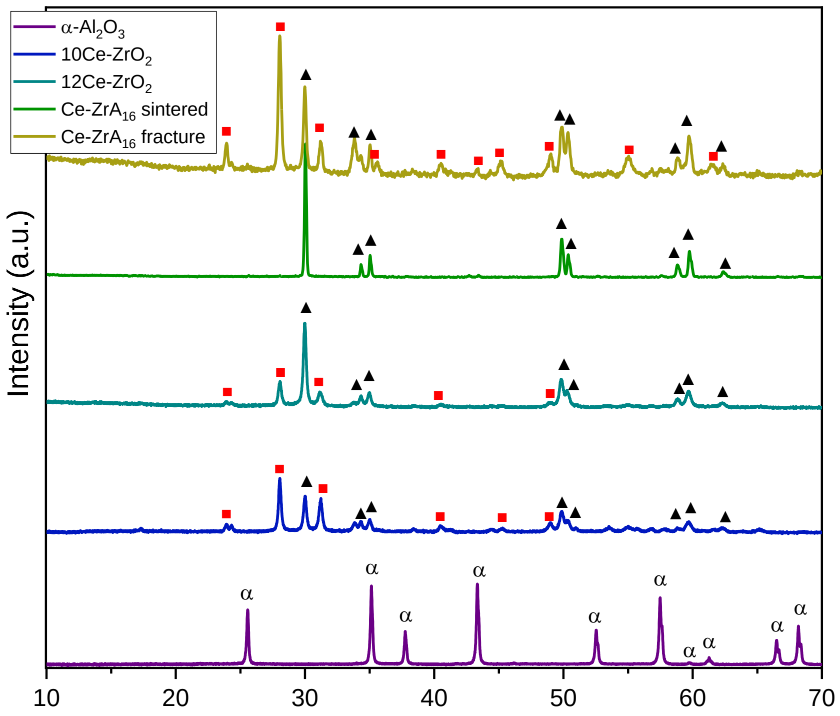

Figure 13: XRD patterns of as-received Al_2O_3, 10Ce-ZrO_2, 12Ce-ZrO_2 and of the Ce-ZA_{16} sintered composite, before and after fracture. α = α-Al_2O_3; ▲= t-ZrO_2; 🟥 = m-ZrO_2

4. Conclusions

In this work, we have successfully fabricated zirconia-alumina parts using a DLP stereolithography-based 3D printing technology. UV-curable ceramic suspensions exhibit shear-thinning behaviour, and the addition of the Disperbyk 103 to the formulation allows the increasing of the solid loading maintaining, at the same time, the ideal rheology and stability. The cure depth increases with the exposure time, which should be controlled to 15 s with a led power of 31.96 mW/cm^2 to guarantee a cure depth that is 1.5 time the layer thickness of 20 μm. FE-SEM observations indicated that the parts were composed of a highly dense and homogeneous microstructure with optimal distribution of the submicron α-Al_2O_3 second phase inside a fine zirconia matrix. The maximum density was achieved at 70 wt%, providing values of 97.3% and 99.4% at 1500 °C/1h and 1550 °C/1h, respectively. The printed and sintered composite showed almost pure tetragonal phase, while XRD performed on a sample fracture surface showed 78% monoclinic phase, suggesting that the stabilizer amount was proper to induce the correct stress-induced phase transformation. Finally, it was also demonstrated that 3D printing is a promising processing technique to build up parts with the desired structure for future developments.

Acknowledgements

The authors gratefully acknowledge the Safety of Infrastructures and Constructions (SISCON) laboratory for providing the instrumentation for thermal and rheological analyses.

5. References

1. Lube, T., Staudacher, M., Hofer, A.-K., Schlacher, J. & Bermejo, R. Stereolithographic 3D printing of ceramics: challenges and opportunities for structural integrity. *Adv. Eng. Mater.* **2200520**, 1–10 (2022).

2. Hannouche, D., Zingg, M., Miozzari, H., Nizard, R. & Lübbeke, A. Third-generation pure alumina and alumina matrix composites in total hip arthroplasty: What is the evidence? *EFORT Open Rev.* **3**, 7–14 (2017).

3. Denry, I. & Kelly, J. R. Emerging ceramic-based materials for dentistry. *J. Dent. Res.* **93**, 1235–1242 (2014).

4. Green, D. J., Hannink, R. H. J. & Swain, M. V. *Transformation toughening of ceramics*. (1989). doi:https://doi.org/10.1201/9781351077408

5. Evans, A. G. & Cannon, R. M. Overview no. 48. Toughening of brittle solids by martensitic transformations. *Acta Metall.* **34**, 761–800 (1986).

6. Chevalier, J., Gremillard, L., Virkar, A. V. & Clarke, D. R. The tetragonal-monoclinic transformation in zirconia: Lessons learned and future trends. *J. Am. Ceram. Soc.* (2009).

doi:10.1111/j.1551-2916.2009.03278.x

7. Piconi, C. & Maccauro, G. Zirconia as a ceramic biomaterial. *Biomaterials* (1999). doi:10.1016/S0142-9612(98)00010-6

8. Tsukuma, K. & Shimada, M. Strength , fracture toughness and Vickers hardness of CeO2-stabilized tetragonal. *J. Mater. Sci. K., Shimada, M. (1985). Strength , Fract. toughness Vickers hardness CeO2-stabilized tetragonal. J. Mater. Sci. 20(1 985), 1178–1184.* **20**, 1178–1184 (1985).

9. Fornabaio, M. *et al.* Zirconia-based composites for biomedical applications: Role of second phases on composition, microstructure and zirconia transformability. *J. Eur. Ceram. Soc.* **35**, 4039–4049 (2015).

10. Palmero, P. *et al.* Towards long lasting zirconia-based composites for dental implants: Part I: Innovative synthesis, microstructural characterization and invitro stability. *Biomaterials* **50**, 38–46 (2015).

11. Reveron, H. *et al.* Towards long lasting zirconia-based composites for dental implants: Transformation induced plasticity and its consequence on ceramic reliability. *Acta Biomater.* **48**, 423–432 (2017).

12. Tulliani, J. M., Lombardi, M., Palmero, P., Fornabaio, M. & Gibson, L. J. Development and mechanical characterization of novel ceramic foams fabricated by gel-casting. *J. Eur. Ceram. Soc.* **33**, 1567–1576 (2013).

13. Sarraf, H., Herbig, R. & Maryška, M. Fine-grained Al2O3-ZrO2 composites by optimization of the processing parameters. *Scr. Mater.* **59**, 155–158 (2008).

14. Echeberria, J. *et al.* Sinter and hot isostatic pressing (HIP) of multi-wall carbon nanotubes (MWCNTs) reinforced ZTA nanocomposite: Microstructure and fracture toughness. *Int. J.*

Refract. Met. Hard Mater. **28**, 399–406 (2010).

15. Wang, S. kun *et al.* Preparation of gradient zta ceramic by centrifugal slip casting method. *Adv. Mater. Res.* **569**, 324–327 (2012).

16. Jiménez-Melendo, M. *et al.* High temperature plastic deformation of multilayered YTZP/ZTA composites obtained by tape casting. *Acta Mater.* **46**, 3995–4004 (1998).

17. Gadow, R. & Kern, F. Pressureless sintering of injection molded zirconia toughened alumina nanocomposites. *J. Ceram. Soc. Japan* **114**, 958–962 (2006).

18. Montanaro, L., Coppola, B., Palmero, P. & Tulliani, J. M. A review on aqueous gelcasting: A versatile and low-toxic technique to shape ceramics. *Ceram. Int.* **45**, 9653–9673 (2019).

19. Deville, S. Freeze-casting of porous ceramics: A review of current achievements and issues. *Adv. Eng. Mater.* **10**, 155–169 (2008).

20. Jabbari, M. *et al.* Ceramic tape casting: A review of current methods and trends with emphasis on rheological behaviour and flow analysis. *Mater. Sci. Eng. B Solid-State Mater. Adv. Technol.* **212**, 39–61 (2016).

21. Cramer, C. L. *et al.* Accuracy of stereolithography printed alumina with digital light processing. *Open Ceram.* **8**, 100194 (2021).

22. Dehurtevent, M. *et al.* Effect of build orientation on the manufacturing process and the properties of stereolithographic dental ceramics for crown frameworks. *J. Prosthet. Dent.* **125**, 453–461 (2021).

23. Wu, H. *et al.* Effect of the particle size and the debinding process on the density of alumina ceramics fabricated by 3D printing based on stereolithography. *Ceram. Int.* **42**, 17290–17294 (2016).

24. Chen, S. *et al.* Effects of particle size distribution and sintering temperature on properties of

alumina mold material prepared by stereolithography. *Ceram. Int.* **48**, 6069–6077 (2022).

25. Shuai, X., Zeng, Y., Li, P. & Chen, J. Fabrication of fine and complex lattice structure Al2O3 ceramic by digital light processing 3D printing technology. *J. Mater. Sci.* **55**, 6771–6782 (2020).

26. Johansson, E., Lidström, O., Johansson, J., Lyckfeldt, O. & Adolfsson, E. Influence of resin composition on the defect formation in alumina manufactured by stereolithography. *Materials (Basel).* **10**, (2017).

27. Liu, W. *et al.* Synergy of solid loading and printability of ceramic paste for optimized properties of alumina via stereolithography-based 3D printing. *J. Mater. Res. Technol.* **9**, 11476–11483 (2020).

28. Xing, H. *et al.* Preparation and characterization of UV curable Al2O3 suspensions applying for stereolithography 3D printing ceramic microcomponent. *Powder Technol.* **338**, 153–161 (2018).

29. Schwarzer, E. *et al.* Process development for additive manufacturing of functionally graded alumina toughened zirconia components intended for medical implant application. *J. Eur. Ceram. Soc.* (2019). doi:10.1016/j.jeurceramsoc.2018.09.003

30. Zhang, K. *et al.* High solid loading, low viscosity photosensitive Al2O3 slurry for stereolithography based additive manufacturing. *Ceram. Int.* **45**, 203–208 (2019).

31. Wang, J. C. & Dommati, H. Fabrication of zirconia ceramic parts by using solvent-based slurry stereolithography and sintering. *Int. J. Adv. Manuf. Technol.* **98**, 1537–1546 (2018).

32. Komissarenko, D. A., Sokolov, P. S., Evstigneeva, A. D., Shmeleva, I. A. & Dosovitsky, A. E. Rheological and curing behavior of acrylate-based suspensions for the DLP 3D printing of complex zirconia parts. *Materials (Basel).* **11**, (2018).

33. Li, H. *et al.* Influence of Vacuum Debinding Temperature on Microstructure and Mechanical Properties of Three-Dimensional-Printed Alumina via Stereolithography. *3D Print. Addit. Manuf.* **7**, 8–18 (2020).

34. Song, S. Y., Park, M. S., Lee, D., Lee, J. W. & Yun, J. S. Optimization and characterization of high-viscosity ZrO2 ceramic nanocomposite resins for supportless stereolithography. *Mater. Des.* **180**, 107960 (2019).

35. Zhang, J. *et al.* Digital light processing-stereolithography three-dimensional printing of yttria-stabilized zirconia. *Ceram. Int.* (2020). doi:10.1016/j.ceramint.2019.12.113

36. Zhang, K. *et al.* Photosensitive ZrO 2 suspensions for stereolithography. *Ceram. Int.* **45**, 12189–12195 (2019).

37. Han, Z. *et al.* A Novel ZrO2 Ceramic Suspension for Ceramic Stereolithography. *IOP Conf. Ser. Mater. Sci. Eng.* **678**, (2019).

38. Borlaf, M., Serra-Capdevila, A., Colominas, C. & Graule, T. Development of UV-curable ZrO2 slurries for additive manufacturing (LCM-DLP) technology. *J. Eur. Ceram. Soc.* (2019). doi:10.1016/j.jeurceramsoc.2019.05.023

39. Rosa, M., Barou, C. & Esposito, V. Zirconia UV-curable colloids for additive manufacturing via hybrid inkjet printing-stereolithography. *Mater. Lett.* **215**, 214–217 (2018).

40. Li, Y. *et al.* Cure behavior of colorful ZrO2 suspensions during Digital light processing (DLP) based stereolithography process. *J. Eur. Ceram. Soc.* **39**, 4921–4927 (2019).

41. Coppola, B., Lacondemine, T., Tardivat, C., Montanaro, L. & Palmero, P. Designing alumina-zirconia composites by DLP-based stereolithography: Microstructural tailoring and mechanical performances. *Ceram. Int.* **47**, 13457–13468 (2021).

42. Zheng, T., Wang, W., Sun, J., Liu, J. & Bai, J. Development and evaluation of Al2O3–ZrO2

composite processed by digital light 3D printing. *Ceram. Int.* **46**, 8682–8688 (2020).

43. Borlaf, M., Szubra, N., Serra-Capdevila, A., Kubiak, W. W. & Graule, T. Fabrication of ZrO2 and ATZ materials via UV-LCM-DLP additive manufacturing technology. *J. Eur. Ceram. Soc.* **40**, 1574–1581 (2020).

44. Wu, H. *et al.* Fabrication of dense zirconia-toughened alumina ceramics through a stereolithography-based additive manufacturing. *Ceram. Int.* (2017). doi:10.1016/j.ceramint.2016.10.027

45. Xing, H. *et al.* Effect of particle size distribution on the preparation of ZTA ceramic paste applying for stereolithography 3D printing. *Powder Technol.* **359**, 314–322 (2020).

46. Cailliet, S., Roumanie, M., Croutxé-Barghorn, C., Bernard-Granger, G. & Laucournet, R. Y-TZP, Ce-TZP and as-synthesized Ce-TZP/Al2O3 materials in the development of high loading rate digital light processing formulations. *Ceram. Int.* **47**, 3892–3900 (2021).

47. Sun, J., Binner, J. & Bai, J. 3D printing of zirconia via digital light processing: optimization of slurry and debinding process. *J. Eur. Ceram. Soc.* **40**, 5837–5844 (2020).

48. Damyanova, S., Pawelec, B., Arishtirova, K., Huerta, M. V. M. & Fierro, J. L. G. Study of the surface and redox properties of ceria-zirconia oxides. *Appl. Catal. A Gen.* **337**, 86–96 (2008).

49. Kambolis, A., Matralis, H., Trovarelli, A. & Papadopoulou, C. Ni/CeO2-ZrO2 catalysts for the dry reforming of methane. *Appl. Catal. A Gen.* **377**, 16–26 (2010).

50. Richardson, R. P. C. and J. F. *Non-Newtonian Flow and Applied Rheology*. *Hypnosis: Developments in Research and New Perspectives* (2008). doi:https://doi.org/10.1016/B978-0-7506-8532-0.X0001-7

51. Li, X. B., Zhong, H., Zhang, J. X., Duan, Y. Sen & Jiang, D. L. Powder Characteristics on

the Rheological Performance of Resin-based Zirconia Suspension for Stereolithography. *Wuji Cailiao Xuebao/Journal Inorg. Mater.* **35**, 231–235 (2020).

52. Wu, Z. *et al.* Research into the mechanical properties, sintering mechanism and microstructure evolution of Al2O3-ZrO2 composites fabricated by a stereolithography-based 3D printing method. *Mater. Chem. Phys.* **207**, 1–10 (2018).

53. Hinczewski, C., Corbel, S. & Chartier, T. Ceramic suspensions suitable for stereolithography. *J. Eur. Ceram. Soc.* **18**, 583–590 (1998).

54. Chevirė, F. *et al.* UV absorption properties of ceria-modified compositions within the fluorite-type solid solution CeO2-Y6WO12. *J. Solid State Chem.* **179**, 3184–3190 (2006).

55. Maring, B. J. & Webley, P. A. A new simplified pressure/vacuum swing adsorption model for rapid adsorbent screening for CO2 capture applications. *Int. J. Greenh. Gas Control* **15**, 16–31 (2013).

56. Li, K. & Zhao, Z. The effect of the surfactants on the formulation of UV-curable SLA alumina suspension. *Ceram. Int.* **43**, 4761–4767 (2017).